

# Comprehensive Study of a $z = 2.35$ DLA Galaxy: Mass, Metallicity, Age, Morphology and SFR from HST and VLT\*

Jens-Kristian Krogager,<sup>1,2†</sup> Johan P. U. Fynbo<sup>1</sup>, Cédric Ledoux<sup>2</sup>, Lise Christensen<sup>1</sup>, Anna Gallazzi<sup>3,1</sup>, Peter Laursen<sup>1</sup>, Palle Møller<sup>4</sup>, Pasquier Noterdaeme<sup>5</sup>, Céline Péroux<sup>6</sup>, Max Pettini<sup>7</sup>, Marianne Vestergaard<sup>1,8</sup>

<sup>1</sup>Dark Cosmology Centre, Niels Bohr Institute, Copenhagen University, Juliane Maries Vej 30, 2100 Copenhagen Ø, Denmark

<sup>2</sup>European Southern Observatory, Alonso de Córdova 3107, Vitacura, Casilla 19001, Santiago 19, Chile

<sup>3</sup>INAF – Osservatorio Astrofisico di Arcetri, Largo Enrico Fermi 5, 50125 Firenze, Italy

<sup>4</sup>European Southern Observatory, Karl-Schwarzschild-Strasse 2, D-85748 Garching bei München, Germany

<sup>5</sup>UPMC-CNRS, UMR7095, Institut d’Astrophysique de Paris, F-75014 Paris, France

<sup>6</sup>Aix Marseille Université, CNRS, LAM (Laboratoire d’Astrophysique de Marseille) UMR 7326, 13388, Marseille, France

<sup>7</sup>Institute of Astronomy, Kavli Institute for Cosmology, Madingley Road Cambridge, CB3 0HA

<sup>8</sup>Steward Observatory, University of Arizona, 933 N Cherry Avenue, Tucson, AZ 85721, USA

Accepted 30 May 2013. Received ; in original form

## ABSTRACT

We present a detailed study of the emission from a  $z = 2.35$  galaxy that causes damped Lyman- $\alpha$  absorption in the spectrum of the background QSO, SDSS J 2222–0946. We present the results of extensive analyses of the stellar continuum covering the rest frame optical-UV regime based on broad-band *HST* imaging, and of spectroscopy from VLT/X-Shooter of the strong emission lines: Ly $\alpha$ , [OII], [OIII], [NII], H $\alpha$  and H $\beta$ . We compare the metallicity from the absorption lines in the QSO spectrum with the oxygen abundance inferred from the strong-line methods (R<sub>23</sub> and N2). The two emission-line methods yield consistent results: [O/H] =  $-0.30 \pm 0.13$ . Based on the absorption lines in the QSO spectrum a metallicity of  $-0.49 \pm 0.05$  is inferred at an impact parameter of 6.3 kpc from the centre of the galaxy with a column density of hydrogen of  $\log(N_{\text{HI}}/\text{cm}^{-2}) = 20.65 \pm 0.05$ . The star formation rates of the galaxy from the UV continuum and H $\alpha$  line can be reconciled assuming an amount of reddening of  $E(B - V) = 0.06 \pm 0.01$ , giving an inferred SFR of  $13 \pm 1 M_{\odot} \text{ yr}^{-1}$  (Chabrier IMF). From the *HST* imaging, the galaxy associated with the absorption is found to be a compact ( $r_e=1.12$  kpc) object with a disc-like, elongated (axis ratio 0.17) structure indicating that the galaxy is seen close to edge-on. Moreover, the absorbing gas is located almost perpendicularly above the disc of the galaxy suggesting that the gas causing the absorption is not co-rotating with the disc. We investigate the stellar and dynamical masses from SED-fitting and emission-line widths, respectively, and find consistent results of  $2 \times 10^9 M_{\odot}$ . We suggest that the galaxy is a young *proto*-disc with evidence for a galactic outflow of enriched gas. This galaxy hints at how star-forming galaxies may be linked to the elusive population of damped Ly $\alpha$  absorbers.

**Key words:** galaxies: formation – galaxies: high-redshift – galaxies: ISM – quasars: absorption lines – quasars: individual: SDSS J 22:22:56.1–09:46:36.2 – cosmology: observations

## 1 INTRODUCTION

Mapping the structure, properties and chemical enrichment of galaxies over cosmic history is a major goal of contemporary astrophysics. In the local Universe, important advances can be made by studying the age-metallicity relation of stars in the Solar neighbourhood (e.g., Holmberg et al. 2007; Caffau et al. 2011) or in local group dwarf galaxies (Frebel et al. 2007, 2010). At redshifts higher than  $z \approx 2$ , a powerful method for studying chemical evolution is spectroscopy of Damped Ly $\alpha$  Absorbers (DLAs) detected either towards background QSOs (see Wolfe et al. 2005, and references

\* Based on observations collected at the European Organisation for Astronomical Research in the Southern Hemisphere, Chile, under program 087.A-0085(A). Based on observations made with the NASA/ESA Hubble Space Telescope, obtained at the Space Telescope Science Institute, which is operated by the Association of Universities for Research in Astronomy, Inc., under NASA contract NAS 5-26555. These observations are associated with program 12553.

† E-mail: krogager@dark-cosmology.dk

therein) or against Gamma-ray Burst (GRB) afterglow light (Fynbo et al. 2006; Savaglio 2006; Prochaska et al. 2007). In those studies, abundances are determined from the gas phase as probed by the H I and metal absorption lines detected against the light of the background QSOs and GRB afterglows, respectively.

Mainly at lower redshifts, but recently also at  $z \gtrsim 2$ , H II-region abundances are determined using the relative strengths of strong emission lines (e.g., Kewley & Ellison 2008; Shapley 2011, and references therein). Currently, there have only been very few cases where both methods have been applied to the same object. The first example is the case of the DLA towards SBS 1543+593 (Bowen et al. 2005) where the two methods yielded consistent results. Since then a handful of other cases have been studied (see the compilation in Péroux et al. 2012). As seen in Fig. 8 of Péroux et al. (2012), the absorption-line measurements generally probe regions at larger galactocentric distances than the emission-line based measurements and on average indicate lower metallicities than the results based on emission-lines, possibly reflecting the early setup of metallicity gradients (O’Rourke et al. 2011). However, it is important to stress that different recipes to derive oxygen abundances using strong emission-line fluxes reveal very inconsistent results (Kewley & Ellison 2008). It is therefore of interest to expand the sample of sources where strong-line based abundances can be independently tested using other methods (see also Pettini 2006; Kudritzki et al. 2012). Also, the use of different elements, e.g., Fe, Zn or Si, to infer absorption metallicities may introduce systematic offsets when comparing galaxies within a heterogeneous sample.

Combining the two complementary methods of studying the metal enrichment in galaxies provides important hints to understanding how galaxies turn their gas into stars, as the absorption lines directly probe the cold gas, and the properties of the star forming region can be probed directly from the emission lines, and sometimes also from the continuum. However, linking the absorption characteristics of DLAs to the emission characteristics of the galaxies causing the absorption has been a great challenge at high redshift, due to the faint nature of DLA galaxies and due to their proximity to a very bright QSO. So far, only a few DLA systems with confirmed emission counterparts have been established at redshifts around and higher than two (Krogager et al. 2012).

Here we present an analysis of the DLA at  $z = 2.35$  with  $\log(N_{\text{HI}}/\text{cm}^{-2}) = 20.65 \pm 0.05$  seen in the spectrum of the  $z = 2.93$  QSO 2222–0946. The galaxy counterpart of the absorber was detected by Fynbo et al. (2010) and here we present new, deeper spectroscopic data allowing us to measure the metallicity directly from nebular [O II], [O III], and Balmer emission lines. Furthermore, we combine the spectroscopic data with imaging from Wide Field Camera 3 (WFC3) onboard the *Hubble Space Telescope* (*HST*). The high resolution images from *HST* makes it possible to detect the continuum emission from the galaxy directly, allowing us to characterize the properties and structure of the absorbing galaxy. This enables us to start bridging the gap between the population of DLA galaxies and star-forming galaxies.

The paper is organized as follows. In Sect. 2, we present the spectroscopic data from X-Shooter and the imaging data from *HST*/WFC3. In Sect. 3, we derive the oxygen abundance from nebular emission lines, derive the gas phase metal abundances, characterize the morphology from the imaging data, and finally we obtain fluxes of the galaxy used for spectral energy distribution (SED) fitting. In Sect. 4, we compare the absorption and emission properties, and discuss and outline the implications of our work. Throughout this paper, we assume a standard  $\Lambda$ CDM cosmology with  $H_0 = 71 \text{ km s}^{-1} \text{ Mpc}^{-1}$ ,  $\Omega_\Lambda = 0.7$  and  $\Omega_M = 0.3$ .

## 2 OBSERVATIONS AND DATA REDUCTION

### 2.1 X-Shooter spectroscopy

QSO 2222–0946 was observed with the X-Shooter spectrograph (Vernet et al. 2011) mounted on ESO’s Very Large Telescope, Unit Telescope 2, for a total of 10 hours and 47 minutes during the nights of 2011 May 14, 2011 August 4, 29, and 30. The integrations were split into ten different exposures each made up of four sub-exposures dithered along the slit. The instrument is composed of three separate spectrographs (so-called arms): UVB covering 330 nm to 560 nm, VIS covering 550 nm to 1020 nm, and NIR covering 1020 nm to 2480 nm. For all observations slit-widths of 0.8, 0.7 and 0.9 arcsec for were used for UVB, VIS and NIR, respectively, and we used the slow readout with  $1 \times 2$  binning, i.e., 2 times binning in the spatial direction. The individual spectra have been processed using the official ESO pipeline (Modigliani et al. 2010) for nodded exposures version (2.0.0). The spectra were individually flux-calibrated using the standard star observed at the beginning of the night for each integration. All spectra were taken during very good conditions with clear sky and good seeing. The error on the flux calibration is on the order of 5%, as determined from the robustness of the calibration when using different standard stars. We note that Fynbo et al. (2010) scale their spectrum of this target to the one available from the Sloan Digital Sky Survey. Given our very robust flux calibration we have chosen to trust the pipeline product. Also, comparison of spectra observed in very different epochs, as is the case here, is not straightforward given the random variability of QSOs. We encountered issues with a too low flux-level of the VIS spectra for unknown reasons. For this reason we scaled the VIS spectra to the overlapping regions of the well-determined UVB and NIR spectra. With a simple multiplicative factor we were able to match both UVB and NIR at the same time. The scaling does not affect any of the extracted emission lines as they are all in the NIR spectra, except for Ly $\alpha$  in the UVB.

The final 2D-spectra were then spatially aligned and added by error-weighting, and we correct for slit-loss by calculating how much light gets dispersed outside the slit at the given seeing in each exposure before co-adding all the observations. We have not corrected for telluric absorption, since those regions are not crucial for our analysis. The effective seeing in the final flux and wavelength calibrated 2D-spectrum is  $0''.7$  (inferred from the width of the trace at 715 nm) and we measure the resolving power in the spectrum from telluric lines to be 11,000 and 7,000 for the VIS and NIR arms, respectively. As there are no direct features in the UVB arm to indicate the resolving power we assume the resolving power in the UVB arm to be the expected 6,200 from the specifications of the X-Shooter manual given a slit width of  $0''.8$ , as the average seeing in UVB was  $0''.77$  (measured at 480 nm).

In Figure 1 the spectrum blue-ward of the QSO Ly $\alpha$  emission line is shown, demonstrating the quality of the combined spectrum; note the significant flux below the Lyman limit at  $z = 2.87$ .

### 2.2 HST / WFC3 imaging

The field was observed with the Wide Field Camera 3 on 2011 Nov 10 (with the UVIS detector in the F606W filter) and on 2012 Sep 14 and 15 (with the IR detector in the F105W and F160W filters). The roll-angle of the telescope was set such that the galaxy counterpart of the DLA fell between the diffraction spikes of the Point Spread Function (PSF). The two observations with the IR detector were taken using the WFC3-IR-DITHER-BOX-MIN pattern providing an

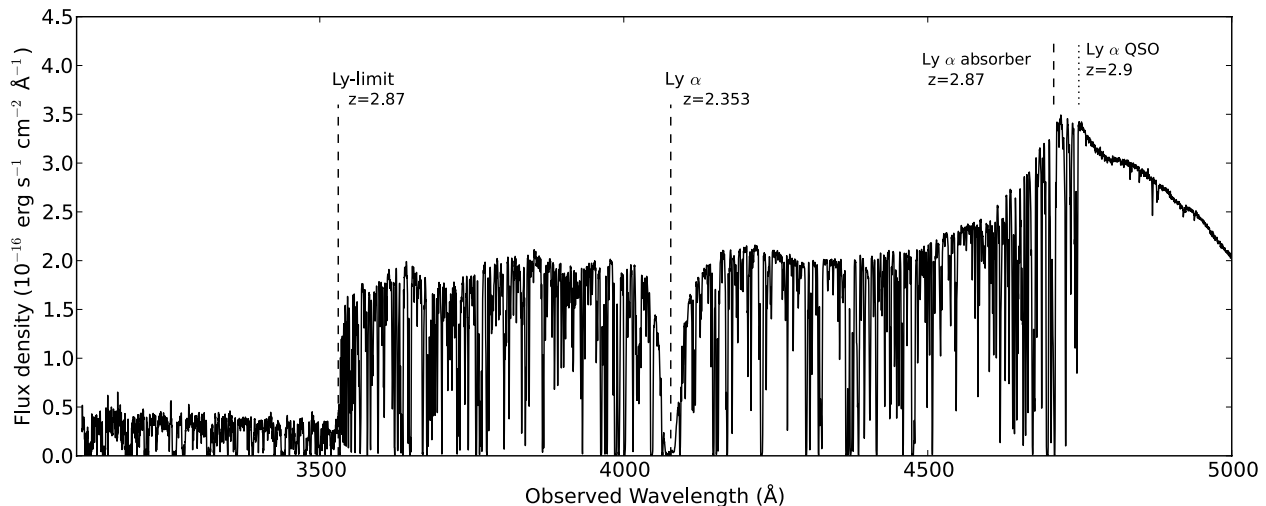


**Figure 1.** The final 1D spectrum from the UVB arm of the  $z = 2.9$  Q 2222–0946. In the left part of the spectrum, the Lyman limit from an absorber at redshift  $z = 2.87$  is clearly seen and the damped Lyman-alpha absorption line is identified in the middle of the figure by the vertical dashed line. The Lyman-alpha emission line at the QSO redshift is seen in the right part of the figure.

optimal 4-point sampling of the PSF. The UVIS observation was taken using the WFC3-UVIS-DITHER-BOX pattern.

The field was observed using a 4-point sub-pixel dither pattern, which allowed us to regain more spatial information. We have used the software package `multidrizzle`<sup>1</sup> to align and combine the images. By shifting and combining the images taken with sub-pixel offsets one achieves a better sampling of the PSF, which in the case of the NIR observations is quite crucial as the PSF is poorly sampled in the native  $0''.13 \text{ px}^{-1}$  images. Furthermore, the drizzle-algorithm allows us to reduce the pixel size when combining the images providing sharper and better sampled images. For the combination in this work we have set the parameter `pixfrac` to 0.7 and used a final pixel scale of  $0''.06 \text{ px}^{-1}$  for NIR and  $0''.024 \text{ px}^{-1}$  for UVIS. For a detailed description of the parameters in the software we refer the user to the `multidrizzle`<sup>1</sup> user manual.

### 3 RESULTS

#### 3.1 Spectral PSF subtraction

In order to detect the faint emission lines from the foreground Damped Lyman- $\alpha$  Absorbing galaxy we needed to subtract the QSO continuum. We did this by modelling the spectral trace and the spectral point spread function (SPSF) as a function of wavelength. The trace position and amplitude were fitted as a function of wavelength in a small ( $84\text{\AA}$ ) region around each emission line from the galaxy, e.g., [O II], [O III], and [N II]. In the same region around the line we estimated the SPSF by averaging the observed spatial profile along the spectral direction. The modelled 2D-spectrum of the QSO was then subtracted from the observed spectrum, and a 1D-spectrum for each line was extracted with the optimal extraction algorithm of Horne (1986). All extracted emission lines are shown in Figure 2.

<sup>1</sup> `multidrizzle` is a product of the Space Telescope Science Institute, which is operated by AURA for NASA.

#### 3.2 Extracting the Emission Lines

We were able to detect emission from Ly $\alpha$ , H $\alpha$ , H $\beta$ , the [O II]  $\lambda\lambda$  3727, 3729 doublet, the two [O III] lines at 4959  $\text{\AA}$  and 5007  $\text{\AA}$ , and [N II]  $\lambda$  6583. The line profiles for all the extracted lines were fitted with Gaussian profiles to measure the flux in the line. The parameters of the Gaussian were allowed to vary in all fits except for [O II] and [N II]. The line-width and redshift of the two [O II] components were tied in the fit, because of a sky line that falls right between the two components. For the very faint [N II]-line, we re-binned the spectrum by a factor of two and fixed the redshift and line-width to the values of the nearby H $\alpha$  line. The errors on the fluxes were estimated by varying the line profile within the error of each fit parameter 1,000 times. The uncertainty was then determined from the  $1\sigma$  width of the resulting distribution of fluxes. The fluxes and errors are listed in Table 1.

All the extracted lines with Gaussian line fits are shown in Fig. 2 along with the best fitting Gaussian profile. The grey shaded areas indicate telluric emission or absorption features. These regions were included in the fits to give the optimal estimate of uncertainties on the fit parameters. The Ly $\alpha$  line is shown in Fig. 3. Due to the asymmetric shape and the complex nature of the resonant line, we determine the line flux simply by integrating the observed line profile as opposed to fitting the line.

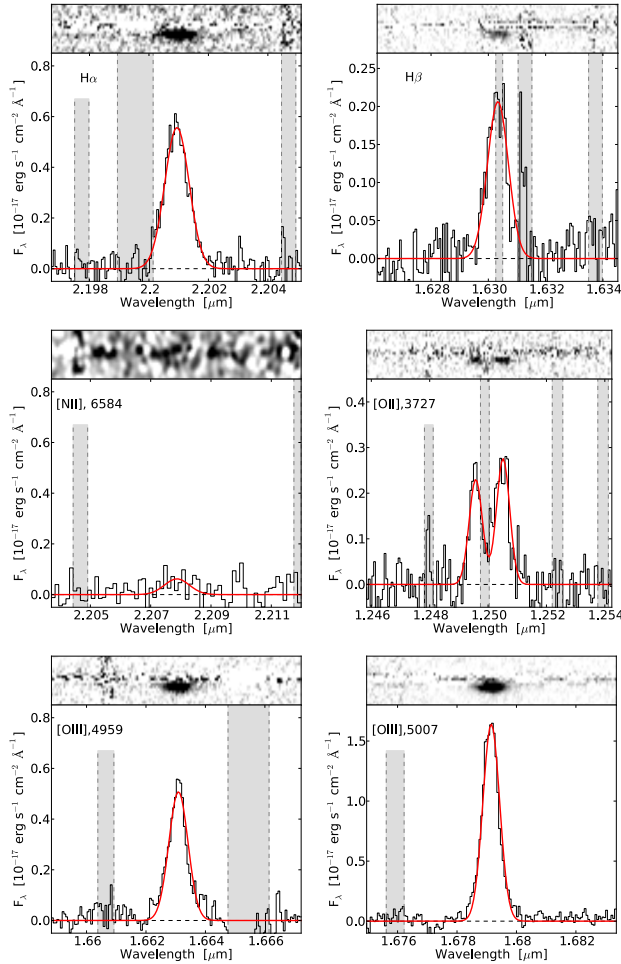
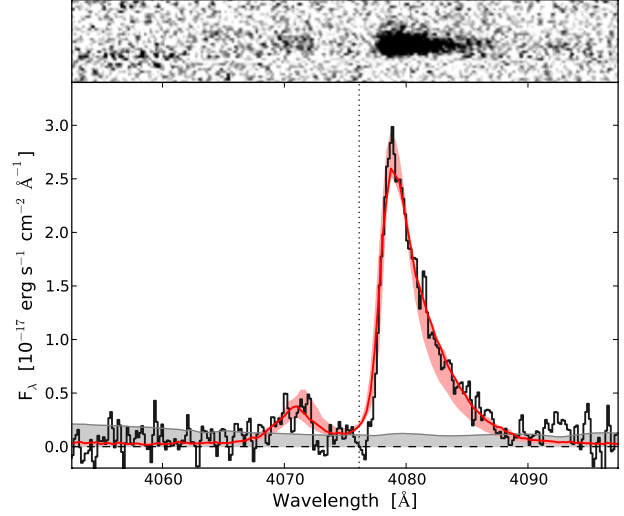
#### 3.3 Balmer Decrement

The ratio of the H $\alpha$  and H $\beta$  line fluxes provides us with information about the dust extinction in the system as we know what this ratio should be intrinsically, given the physical conditions of the emitting region. Assuming case B recombination with an electron temperature of  $T_e = 10^4 \text{ K}$  and density of  $n_e = 10^2 \text{ cm}^{-3}$ , which are standard assumptions in the literature for star forming regions, the line ratio has a value of 2.86. Requiring that our measured line ratio, after reddening, and the intrinsic ratio be the same, we estimate the reddening:

$$E(B - V) = \frac{2.5}{k(\text{H}\beta) - k(\text{H}\alpha)} \log \left( \frac{(\text{H}\alpha/\text{H}\beta)_{\text{obs}}}{(\text{H}\alpha/\text{H}\beta)_0} \right),$$

**Table 1.** Measured emission line fluxes

Transition	Wavelength <sup>(1)</sup>	Flux <sup>(2)</sup>	FWHM <sup>(3)</sup>	$z$
Ly $\alpha$	1215.67	14.3 $\pm$ 0.3	–	–
[O II]	3726.03, 3728.82	2.9 $\pm$ 0.3	121 $\pm$ 8	2.3536
H $\beta$	4861.33	1.9 $\pm$ 0.2	151 $\pm$ 15	2.3537
[O III]	4958.92	4.1 $\pm$ 0.3	129 $\pm$ 5	2.3537
[O III]	5006.84	11.6 $\pm$ 0.6	110 $\pm$ 2	2.3537
H $\alpha$	6562.80	5.7 $\pm$ 0.3	124 $\pm$ 4	2.3537
[N II]	6583.41	0.6 $\pm$ 0.2	–	–

(1) Transition rest frame wavelength in  $\text{\AA}$ .(2) Flux in units of  $10^{-17} \text{ erg s}^{-1} \text{ cm}^{-2}$ , before reddening correction.(3) Line width at FWHM in units of  $\text{km s}^{-1}$  corrected for the instrumental resolution of  $45 \text{ km s}^{-1}$ .**Figure 2.** Emission lines extracted after the subtraction of the QSO continuum in the 2D spectrum. Each panel shows the 2D spectrum where the horizontal residuals from the QSO subtraction is seen (*top*) and the extracted 1D spectrum of the line (*bottom*). The wavelengths are given in  $\mu\text{m}$  and all flux-density units are  $10^{-17} \text{ erg s}^{-1} \text{ cm}^{-2} \text{ \AA}^{-1}$ . The red line in each panel indicates the best fitting Gaussian to the line profile. The grey filled areas indicate skylines or telluric absorption features.**Figure 3.** The Ly $\alpha$  emission line extracted from the DLA trough in the X-shooter spectrum. The top panel shows the observed 2D spectrum and the panel below shows the extracted 1D spectrum, and  $1\sigma$  uncertainty (grey shaded area). The dotted vertical line shows the systemic line centre. The common asymmetric line shape of Ly $\alpha$  is seen in this case, where the blue-shifted part of the line is heavily absorbed. On top of the observed spectrum the best fitting model of the emission profile is shown (red line) along with the 68% confidence interval (red shaded area), see Sect. 3.7 for details.

where  $k$  denotes the reddening law evaluated at the given wavelength and  $(\text{H}\alpha/\text{H}\beta)_0$  indicates the intrinsic line ratio. We use the extinction law from Calzetti et al. (2000) to quantify the extinction while adopting a  $R_V$  value of 4.05. From the measured ratio in our spectrum of  $(\text{H}\alpha/\text{H}\beta)_{\text{obs}} = 3.03 \pm 0.34$  we obtain the corresponding extinction of  $E(B - V) = 0.05 \pm 0.10$ . In this calculation we have not taken into account effects from differential slit-loss, which arise from the wavelength dependence of the seeing and atmospheric dispersion. The slit loss is greater at lower wavelengths, i.e., for the H $\beta$  line in the case of the Balmer line ratio. However, the effect in the  $K$ - and  $H$ -band, where we extract the Balmer lines, is minor ( $\sim 2\%$ ) compared to the uncertainty introduced by the sky lines, especially at the position of the H $\beta$ -line.

### 3.4 Metallicity

We have inferred the metallicity of the system using three independent methods; two measures of the emission-line metallicity using the strong line ratios  $R_{23}$  and  $N2$ , respectively, and one measure of the absorption-line metallicity from Voigt-profile fitting. In the next sections we present each determination in detail.

#### 3.4.1 $R_{23}$ calibration

We determined the metallicity  $12 + \log(\text{O}/\text{H})$  by use of the strong line diagnostic,  $R_{23}$  (Pagel et al. 1979), defined as the ratio  $([\text{O II}] \lambda\lambda 3727, 3729 + [\text{O III}] \lambda 4959 + [\text{O III}] \lambda 5007) / \text{H}\beta$ . One complication of using this diagnostic is that the metallicity is double-valued for a given value of  $R_{23}$  (the so-called *upper* and *lower* branches). However, due to our relatively high value of  $R_{23}$  we are in the region of the diagram where the two branches are close to one another. The calibration by Kobulnicky

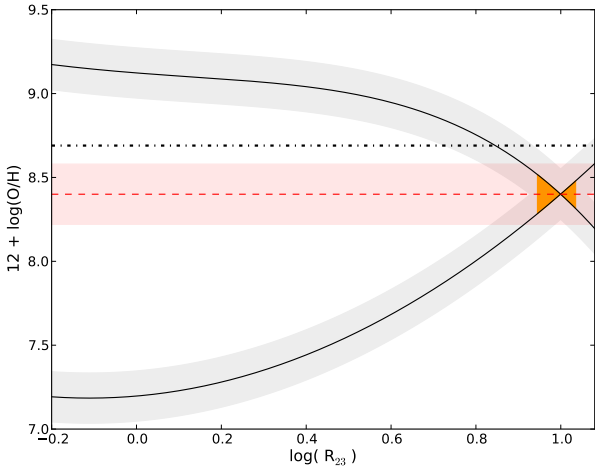


**Figure 4.** Plot of the  $R_{23}$  strong line ratio using the calibration by Kobulnicky & Kewley (2004) (two solid lines) with model uncertainty of 0.15 dex indicated by the light grey shaded area around the curves. The orange filled area between the two solid lines indicates the constraint from our measurement of  $R_{23}$ . The dashed line indicates the inferred metallicity of  $12 + \log(\text{O}/\text{H}) = 8.41$  and the red shaded area around it indicates the  $1\sigma$  uncertainty of 0.19 dex. The dot-dashed line shows the Solar oxygen abundance of  $12 + \log(\text{O}/\text{H})_{\odot} = 8.69$  (Asplund et al. 2009).

& Kewley (2004) that we use depends on the ionization parameter,  $q$ , which can be determined by using the line ratio  $\text{O}_{32} = [\text{O III}] \lambda 5007 / [\text{O II}] \lambda 3727$ , but requires prior knowledge of the metallicity. Given the two measured quantities,  $R_{23}$  and  $\text{O}_{32}$ , we can solve for both metallicity and  $q$  at the same time by iterating the two expressions given an initial guess of metallicity.

From our spectrum we measure  $\log(R_{23}) = 1.00 \pm 0.05$  and  $\log(\text{O}_{32}) = 0.55 \pm 0.05$ . These line ratios are corrected for reddening as indicated by the Balmer decrement. However, in Sect. 3.8 we infer  $E(B - V) = 0.06 \pm 0.01$ , which is the value that we have adopted for the correction here. We perform the iterative calculation of metallicity 500 times while varying the two line-ratios ( $R_{23}$  and  $\text{O}_{32}$ ) within their respective errors. The metallicity and uncertainty is then determined as the median and standard deviation of the resulting distribution. This in turn yields an inferred metallicity of  $12 + \log(\text{O}/\text{H}) = 8.41 \pm 0.19$ , see Fig. 4. We furthermore note that the result does not depend on the initial guess, and that the model uncertainty introduced by the error on the ionization parameter,  $q$ , is negligible. The uncertainty of 0.19 dex includes the contribution from the scatter in the  $R_{23}$  calibration which we conservatively set to 0.15 dex.

### 3.4.2 $N2$ calibration

Our detection of  $[\text{N II}]$  enables us to infer the metallicity independently from the  $N2$  index ( $[\text{N II}] / \text{H}\alpha$ ) as this line ratio has been found to correlate with metallicity (Pettini & Pagel 2004). The calibration from these authors give  $12 + \log(\text{O}/\text{H}) = 8.90 + 0.57 \cdot \log(N2)$  with a scatter of  $\pm 0.18$  dex. The small wavelength difference of  $\text{H}\alpha$  and  $[\text{N II}]$  means that we do not need to worry about reddening effects in the  $N2$  ratio. The measured line fluxes yield a line ratio of  $N2 = 0.11 \pm 0.03$ , giving an inferred metallicity of  $12 + \log(\text{O}/\text{H}) = 8.36 \pm 0.19$ .

Péroux et al. (2012) infer an upper limit of  $12 + \log(\text{O}/\text{H}) < 8.2$

from their non-detection of  $[\text{N II}]$ . Our measurement is slightly higher, but still consistent with theirs within the uncertainties.

Since the two measures of the emission metallicity,  $R_{23}$  and  $N2$ , are independent we can combine both measures to obtain a more precise estimate of  $12 + \log(\text{O}/\text{H}) = 8.39 \pm 0.13$ . Adopting the Solar abundance presented by Asplund et al. (2009) this gives us  $[\text{O}/\text{H}] = -0.30 \pm 0.13$ .

### 3.5 Absorption-line Abundances

In the following section we present detailed measurements of the absorption-line abundances detected in the DLA system. Fynbo et al. (2010) present an analysis of the metal absorption-line system of this DLA using a three-component Voigt-profile fit. They derive fairly high metallicities from  $[\text{Zn}/\text{H}] = -0.46 \pm 0.07$ ,  $[\text{Si}/\text{H}] = -0.51 \pm 0.06$ , and  $[\text{S}/\text{H}] = -0.6 \pm 0.1$ , and see evidence for dust depletion from  $[\text{Mn}/\text{H}] = -1.23 \pm 0.06$ ,  $[\text{Ni}/\text{H}] = -0.85 \pm 0.06$ , and  $[\text{Fe}/\text{H}] = -0.99 \pm 0.06$ . Since our data have much better resolution (recall values in Section 2.1 compared to  $R = 4700, 6700, 4400$  in the Fynbo et al. study for the UVB, VIS and NIR arms, respectively) and much higher Signal-to-Noise Ratio ( $\text{SNR} \sim 100$ , compared to their  $\text{SNR} \sim 50$ ) we can alleviate the effect of hidden saturation, thereby further constraining the metal abundances.

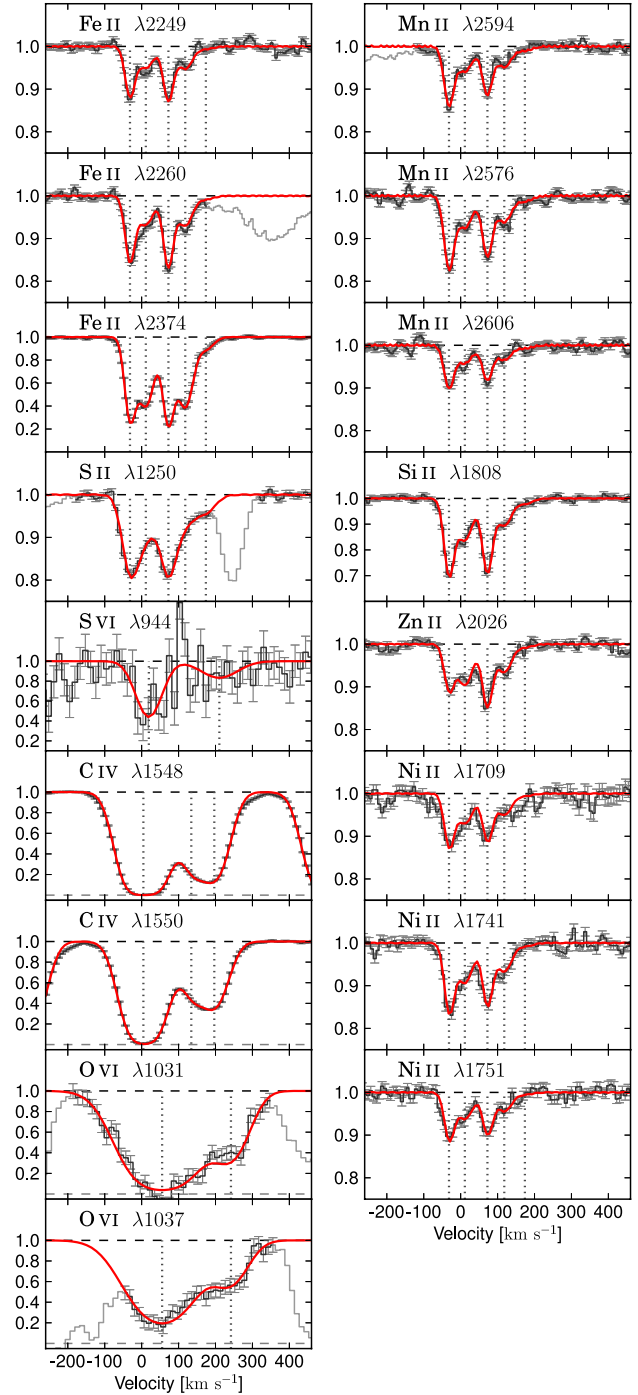
In order to properly decompose the absorption profiles in different velocity components we have selected unsaturated, but well-defined low-ionization lines to infer the metallicity of the absorbing gas (see Fig. 5). Furthermore, we have access to a few high-ionization lines:  $\text{CIV} \lambda\lambda 1548, 1550$ ,  $\text{OVI} \lambda\lambda 1031, 1037$ , and possibly  $\text{SVI} \lambda 944$ . We have ignored the  $\text{Cr II} \lambda 2066$  line because it is heavily blended with telluric absorption features. We found that a five-component fit provides a satisfactory description of the low-ionization lines. All the lines were fitted simultaneously using `FitLyman` in `MIDAS` (Fontana & Ballester 1995) while tying the broadening parameter,  $b$ , and the redshift for each velocity component for all lines. The results for the individual components of the fit are summarized in Table 2. We derive the total column densities from the fit by adding the column densities for all components of each species. These and the derived metallicities are listed in Table 3. For the  $\text{Ti II} \lambda\lambda 1910$  doublet we get an upper limit ( $3\sigma$ ) of  $[\text{Ti}/\text{H}] \leq -0.1$ , as the line is shallow and the continuum level in this part of the spectrum is uncertain. The abundance of  $\text{Zn}$  is probably overestimated due to blending with the weak  $\text{Mg I} \lambda 2826$  line. However, from the  $\text{Mg I} \lambda 2852$  line we are able to constrain the amount of contamination from  $\text{Mg I}$  to be  $\sim 0.1$  dex.

The inferred metallicities are in very good agreement with those determined by Fynbo et al. (2010). The uncertainty of our metallicities, which we estimate to be 0.05 dex from the variance in the data, is dominated by the uncertainty on the normalization of the QSO continuum.

For the high-ionization lines, we have let the redshifts and broadening parameters vary freely for each species. We used three components to fit  $\text{CIV}$  whereas we used two components for the more noisy  $\text{OVI}$  and  $\text{SVI}$  lines. The results from the fit are listed in the bottom part of Table 2. Our possible detection of  $\text{SVI}$  is quoted as an upper limit, and the first component of  $\text{CIV}$  is quoted as a lower limit since the line is saturated. The velocity of the main component of  $\text{CIV}$  is fully consistent with the systemic velocity from the emission lines within the uncertainty of  $9 \text{ km s}^{-1}$ . The oxygen and sulfur lines have slightly larger offsets relative to the emission redshift of  $+20 \text{ km s}^{-1}$  and  $+55 \text{ km s}^{-1}$ , respectively.

**Table 2.** Ionic column densities for individual absorption components of low-ionization lines (top) and high-ionization lines (bottom). The errors quoted below only include the formal errors from `FitLyman`.

Component <sup>1</sup>	$\log(N/\text{cm}^{-2})$	$b$ $\text{km s}^{-1}$
<b>Low-ionization lines</b>		
Si II $\lambda$ 1808		
$v = -32 \text{ km s}^{-1}$	$15.11 \pm 0.01$	$9.1 \pm 0.1$
$v = 11 \text{ km s}^{-1}$	$14.97 \pm 0.01$	$24.0 \pm 0.2$
$v = 73 \text{ km s}^{-1}$	$15.10 \pm 0.01$	$10.1 \pm 0.1$
$v = 118 \text{ km s}^{-1}$	$14.73 \pm 0.02$	$21.6 \pm 0.3$
$v = 174 \text{ km s}^{-1}$	$14.05 \pm 0.07$	$23.7 \pm 1.5$
S II $\lambda$ 1250		
$v = -32 \text{ km s}^{-1}$	$14.80 \pm 0.01$	$9.1 \pm 0.1$
$v = 11 \text{ km s}^{-1}$	$14.56 \pm 0.02$	$24.0 \pm 0.2$
$v = 73 \text{ km s}^{-1}$	$14.82 \pm 0.01$	$10.1 \pm 0.1$
$v = 118 \text{ km s}^{-1}$	$14.35 \pm 0.03$	$21.6 \pm 0.3$
$v = 174 \text{ km s}^{-1}$	$14.18 \pm 0.04$	$23.7 \pm 1.5$
Mn II $\lambda\lambda$ 2576, 2594, 2606		
$v = -32 \text{ km s}^{-1}$	$12.41 \pm 0.01$	$9.1 \pm 0.1$
$v = 11 \text{ km s}^{-1}$	$12.21 \pm 0.01$	$24.0 \pm 0.2$
$v = 73 \text{ km s}^{-1}$	$12.33 \pm 0.01$	$10.1 \pm 0.1$
$v = 118 \text{ km s}^{-1}$	$12.09 \pm 0.01$	$21.6 \pm 0.3$
$v = 174 \text{ km s}^{-1}$	$11.43 \pm 0.05$	$23.7 \pm 1.5$
Fe II $\lambda\lambda\lambda$ 2249, 2260, 2374		
$v = -32 \text{ km s}^{-1}$	$14.59 \pm 0.01$	$9.1 \pm 0.1$
$v = 11 \text{ km s}^{-1}$	$14.39 \pm 0.01$	$24.0 \pm 0.2$
$v = 73 \text{ km s}^{-1}$	$14.64 \pm 0.01$	$10.1 \pm 0.1$
$v = 118 \text{ km s}^{-1}$	$14.38 \pm 0.01$	$21.6 \pm 0.3$
$v = 174 \text{ km s}^{-1}$	$13.46 \pm 0.02$	$23.7 \pm 1.5$
Ni II $\lambda\lambda\lambda$ 1709, 1741, 1751		
$v = -32 \text{ km s}^{-1}$	$13.49 \pm 0.01$	$9.1 \pm 0.1$
$v = 11 \text{ km s}^{-1}$	$13.41 \pm 0.02$	$24.0 \pm 0.2$
$v = 73 \text{ km s}^{-1}$	$13.45 \pm 0.01$	$10.1 \pm 0.1$
$v = 118 \text{ km s}^{-1}$	$13.23 \pm 0.02$	$21.6 \pm 0.3$
$v = 174 \text{ km s}^{-1}$	$12.31 \pm 0.21$	$23.7 \pm 1.5$
Zn II $\lambda$ 2026		
$v = -32 \text{ km s}^{-1}$	$12.14 \pm 0.01$	$9.1 \pm 0.1$
$v = 11 \text{ km s}^{-1}$	$12.29 \pm 0.01$	$24.0 \pm 0.2$
$v = 73 \text{ km s}^{-1}$	$12.31 \pm 0.01$	$10.1 \pm 0.1$
$v = 118 \text{ km s}^{-1}$	$12.08 \pm 0.02$	$21.6 \pm 0.3$
$v = 174 \text{ km s}^{-1}$	$11.16 \pm 0.15$	$23.7 \pm 1.5$
<b>High-ionization lines</b>		
C IV $\lambda\lambda$ 1548, 1550		
$v = 5 \text{ km s}^{-1}$	$>15.23$ <sup>2</sup>	$46.7 \pm 0.3$
$v = 134 \text{ km s}^{-1}$	$14.11 \pm 0.02$	$28.0 \pm 1.4$
$v = 197 \text{ km s}^{-1}$	$14.34 \pm 0.01$	$36.5 \pm 0.8$
O VI $\lambda\lambda$ 1031, 1037		
$v = 55 \text{ km s}^{-1}$	$15.24 \pm 0.02$	$105 \pm 6$
$v = 242 \text{ km s}^{-1}$	$14.49 \pm 0.08$	$54 \pm 10$
S VI $\lambda$ 944		
$v = 20 \text{ km s}^{-1}$	$\leq 14.1 \pm 0.1$ <sup>3</sup>	$35 \pm 9$
$v = 210 \text{ km s}^{-1}$	$\leq 13.6 \pm 0.2$ <sup>3</sup>	$61 \pm 33$

<sup>1</sup> The velocity,  $v$ , indicated at each component shows the relative velocity with respect to the emission redshift  $z = 2.3537$ .<sup>2</sup> Lower limit due to saturation.<sup>3</sup> Upper limit due to possible blending.**Figure 5.** Results of Voigt-profile fitting to the metal absorption lines. The zero point of the velocity scale is fixed to the redshift from the emission lines,  $z_{\text{em}} = 2.3537$  with an uncertainty of  $9 \text{ km s}^{-1}$ . The figure shows the normalized spectra around each fitted line. The part of the spectrum plotted in light grey without error-bars in the panels of Mn II  $\lambda$ 2594, S II  $\lambda$ 1250, Fe II  $\lambda$ 2260, and O VI  $\lambda\lambda$ 1031,1037 shows absorption unrelated to the given line.

**Table 3.** Total column densities and metallicities for the low-ionization lines in the  $z = 2.354$  absorbing system.

Element	$\log(N_X/\text{cm}^{-2})$	[X/H]	$\log(N_\odot/\text{cm}^{-2})$
H	$20.65 \pm 0.05$	–	12.00
Si	$15.62 \pm 0.01$	$-0.54 \pm 0.05$	7.51
S	$15.31 \pm 0.01$	$-0.49 \pm 0.05$	7.15
Mn	$12.89 \pm 0.01$	$-1.19 \pm 0.05$	5.43
Fe	$15.13 \pm 0.01$	$-1.02 \pm 0.05$	7.50
Ni	$14.02 \pm 0.01$	$-0.85 \pm 0.05$	6.22
Zn	$12.83 \pm 0.01$	$-0.38 \pm 0.05$	4.56

Solar abundances are taken from Asplund et al. (2009).

### 3.5.1 Molecular hydrogen

Our data exhibit a number of dips at the expected position of  $\text{H}_2$  lines at  $z_{\text{abs}} = 2.354$ , which suggest a detection of molecular hydrogen at the level of  $\log(N_{\text{H}_2}/\text{cm}^{-2}) \sim 14$ . However, asserting the presence of  $\text{H}_2$  and deriving accurate column densities or limits requires much higher spectral resolution data than what we have available here (see, e.g., Ledoux et al. 2003; Noterdaeme et al. 2008). This is needed in order to (i) deblend the possible  $\text{H}_2$  lines from the Lyman- $\alpha$  forest, (ii) estimate the true continuum of the QSO from unabsorbed spectral regions, and (iii) resolve the velocity structure of the system. Fynbo et al. (2011) reported the detection of  $\text{H}_2$  lines at a resolving power of  $R = 6400$  in the  $z_{\text{abs}} = 2.58$  DLA towards SDSS J0918+1636, but the absence of strong damping wings makes the column density estimates uncertain ( $\log N(\text{H}_2) \sim 16 - 19$ ). The present tentative detection of  $\text{H}_2$  lines towards SDSS J2222–0946 and the corresponding column densities should therefore be verified via follow-up high resolution spectroscopy (i.e.,  $R \gtrsim 50,000$ ).

### 3.6 Structural Fitting of the *HST* images

We started out by modelling the Point Spread Function in each image using the software TINYTIM to create sub-sampled PSFs simulated for each of the individual frames at each position in the four-point dither pattern. We preferred this approach over using stellar sources as the TINYTIM PSFs are more sensitive to the outer regions of the PSF, where the stellar sources are dominated by noise in the sky background.

After resampling the modelled PSFs to the native pixel size and convolving with the filter-specific Charge Diffusion Kernel, these “raw” PSF images were drizzled together in the same way as the actual data to replicate the effect of `multidrizzle` on the PSF shape. We were not able to simulate the PSFs for the infrared images properly because the images were mildly saturated. We therefore chose to use stellar PSFs generated by median combination of stars in the field. Since there are only a handful isolated stars in the field of view with signal-to-noise ratios similar to that of the QSO, we used a few stars with slightly lower SNR in order to reduce the background noise in the PSF.

We used the software GALFIT (Peng et al. 2002) to subtract the QSO and to characterize the absorbing galaxy. Using the modelled PSF for the F606W image we first subtracted the QSO by simply modelling it as a point source while modelling a constant sky background. We then located the nearby galaxy in the residuals. Hereafter, we re-did the fit, this time simultaneously fitting the QSO, the background, and the galaxy using a Sérsic surface bright-

ness profile:

$$\Sigma(r) = \Sigma_e \exp \left[ -\kappa \left( \left( \frac{r}{r_e} \right)^{1/n} - 1 \right) \right],$$

where  $\Sigma_e$  is the surface brightness at the effective radius,  $r_e$ , defined as the radius enclosing half the flux. The Sérsic index,  $n$ , determines the concentration of the profile, with high  $n$  profiles having steeper inner slopes and larger extended wings. The opposite is the case for low  $n$ . The parameter  $\kappa$  is linked to  $n$  to ensure that half of the light is enclosed within the effective radius. The software GALFIT uses a 2D Sérsic profile allowing for elliptical isophotes. The output from fitting the Sérsic profile is given in terms of the total flux from the integrated profile, the effective semi-major axis,  $a_e$ , the Sérsic index,  $n$ , the axis ratio of semi-major and -minor axes,  $b/a$ , and the angle of  $a_e$  with respect to the image-axes. We fitted the galaxy allowing all parameters to vary freely. This resulted in the following best-fitting parameters:  $\text{mag}_{\text{AB}} = 24.29 \pm 0.04$ ,  $n = 0.95 \pm 0.15$ ,  $a_e = 5.80 \pm 0.30$  px,  $b/a = 0.17 \pm 0.02$ , and  $\text{PA} = -26.45 \pm 1.34^\circ$  in the F606W image.

Due to the broader PSF in the NIR images the QSO light is spatially overlapping with the galaxy. We therefore fixed the structural parameters in the Sérsic fit of the galaxy to those of the well-constrained F606W fit. We note that simply locking all structural parameters of the Sérsic profile in the NIR images might not give the most accurate description of the galaxy, as parameters such as size and  $n$  depend on wavelength and thus yield different results when analysed in different wavelength band-passes (Kelvin et al. 2012). However, in order to obtain the most reliable fluxes and to get the fit to converge we had to keep the variables fixed. In order to estimate how robust our obtained fluxes are with respect to the parameters that were held fixed, we varied the Sérsic parameters within their errors (as given by the fit to F606W) and re-did the fit for each new set of profile parameters. The uncertainty on the flux was very minor (0.03 dex) compared to the large uncertainty caused by the PSF subtraction ( $\sim 0.2$  dex). All the obtained magnitudes are listed in Table 4.

In Fig. 6 we show the WFC3 images in the three filters and the residuals after subtracting the modelled QSO PSF. All images are rotated to have North up and East left. The galaxy causing the DLA seen in the QSO spectrum is located to the North-East of the QSO. The red circle in the F105W and F160W images indicates the position of the galaxy from the F606W image. The identification is based on the fact that the position is consistent with the measured offset between the QSO trace and the emission lines in the X-shooter spectrum. The impact parameter of the galaxy with respect to the background quasar is  $0''.74$  corresponding to a projected distance of 6.3 kpc at  $z = 2.354$ , and the angle between the major axis of the galaxy and the line connecting the QSO to the central region of the galaxy is  $71 \pm 2^\circ$ .

### 3.7 Ly $\alpha$ emission modeling

We observe a typical, double-peaked Ly $\alpha$  emission line, with a strong component redwards of line centre and a less prominent blue component (Fig. 3). The large difference between the two peaks indicates that the Ly $\alpha$  photons escape through an expanding medium, and the purpose of this section is to investigate what constraints we can put on the outflow velocity,  $V_{\text{out}}$ . Qualitatively we can see that the red wing extends to several hundreds of  $\text{km s}^{-1}$ . However, in order to get a more accurate description of the emission profile we

**Table 4.** Results from GALFIT analysis

FILTER	mag [AB]	$a_e$ / kpc	$n$	$b/a$
F606W	$24.29 \pm 0.04$	$1.12 \pm 0.06$	$0.95 \pm 0.15$	$0.17 \pm 0.02$
F105W	$24.51 \pm 0.21$	1.12*	0.95*	0.17*
F160W	$23.53 \pm 0.13$	1.12*	0.95*	0.17*

\* Parameters that were fixed in the corresponding fit.

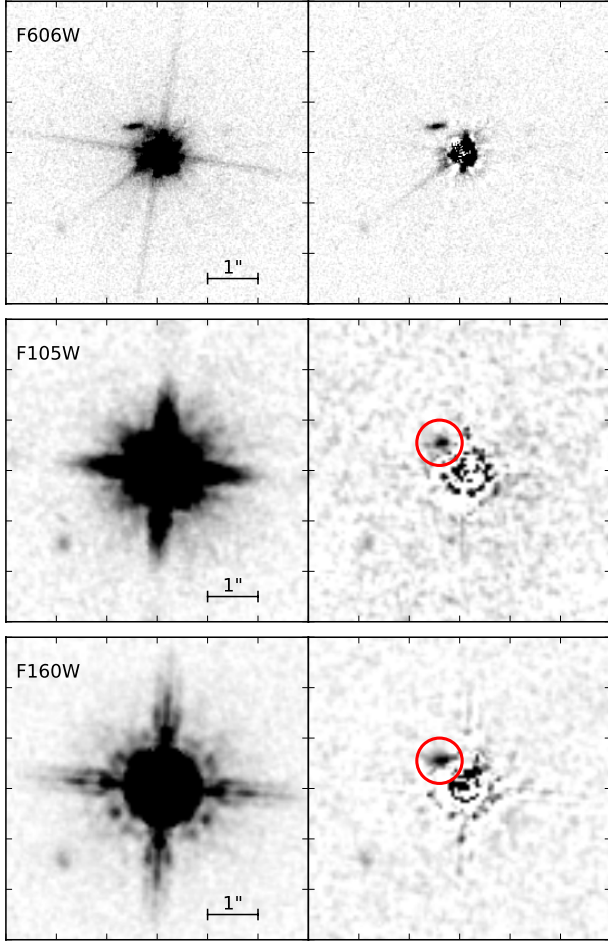


**Figure 6.** Data images (*left*) and PSF-subtracted residuals (*right*) from GALFIT in all three filters. All images are aligned North up and East left. The galaxy causing the absorption is clearly visible in the F606W image even before PSF subtraction. The same position is shown by the red circle in the IR images.

have constructed a semi-realistic model of the system and run Ly $\alpha$  radiative transfer (RT) through it, to find the best-fitting spectrum. The RT is conducted using the code MOCALATA (Laursen et al. 2009a,b), while the galaxy model is similar to the one described in (Laursen et al. 2013). In short, the galaxy is modelled as a sphere of multiphase gas, with warm, neutral clouds floating in a hot, predominantly ionized medium. A similar procedure was used in Noterdaeme et al. (2012), although here we employ a more rigorous approach.

A high number of parameters dictate the outcome of such a simulation. Luckily, our observations offer excellent constraints on many of these: The effective radius,  $r_e = 1.12$  kpc, used to model the size of the emitting region, the metallicity  $Z \simeq 0.31Z_\odot$  (we assume that the amount of metals that condense to dust is similar to the local Universe (Zafar & Watson 2013)), and an average of  $130 \text{ km s}^{-1}$  from the measured emission-line widths are used as a proxy for the intrinsic Ly $\alpha$  line width. From the widths of the low-ionization absorption lines, we use a velocity dispersion of the clouds of  $115 \text{ km s}^{-1}$ . Finally, we infer an intrinsic equivalent width of  $150 \text{ \AA}$ , in accordance with the F606W magnitude. For details on the rest of the parameters, e.g., cloud size distribution, temperatures and densities of the two phases, etc., see Laursen et al. (2013).

We set  $r_{\text{gal}} = 10$  kpc, but note that the exact size of the system is not important, rather the total column density ( $N_{\text{HI}}$ ) from the centre and out, averaged over all directions, determines the shape of the spectrum. This leaves us with two unknown parameters,  $\langle N_{\text{HI}} \rangle$  and  $V_{\text{out}}$ , where  $\langle N_{\text{HI}} \rangle$  is dominated by the number of clouds ( $N_{\text{cl}}$ ). We first run a rough fit to the spectrum, providing us with information about the initial conditions for the system:  $N_{\text{cl}} = 10^5$  and  $V_{\text{out}} = 150 \text{ km s}^{-1}$ , and consequently run a grid of  $11 \times 11$  models with  $N_{\text{cl}} \in [10^{4.5}, 10^{5.5}]$  and  $V_{\text{out}} \in [100, 200] \text{ km s}^{-1}$ .

Instead of doing a regular  $\chi^2$  minimization of the pixel-wise difference between model and spectrum, we compare the observed and the simulated spectra using the following four observables: The peak separation in  $\text{\AA}$ ; the width of the red peak in  $\text{\AA}$ ; the ratio of the integrated flux in the two peaks; and the ratio of the peak heights. The best fit is defined as the model which minimizes all of the four above mentioned criteria simultaneously, given the constraints on metallicity, emission line velocity dispersion, Ly-alpha flux and structure of the emitting region. From the best fit, we find an outflow velocity of  $V_{\text{out}} = 160_{-40}^{+20} \text{ km s}^{-1}$ . Here, the confidence intervals are given by the range of models, for which *all* four estimators lie within the 68% confidence interval of those observed in our spectrum. In the best-fitting model, the average column density and number of clouds intercepted by a sightline towards the QSO at a distance of 6.3 kpc are  $\log(N_{\text{HI}}/\text{cm}^{-2}) = 20.23_{-1.15}^{+0.27}$  and  $n_c = 2 \pm 1$ , respectively. This is somewhat lower although not inconsistent with the measured value of  $20.65 \pm 0.05$  and the fact that five absorption profiles were used in Sect. 3.5.

The escape fraction of Ly $\alpha$  photons ( $f_{\text{esc}} \sim 90\%$ ) is higher than what is found when comparing the total Ly $\alpha$ -to-H $\alpha$  ratio, and we find that a SFR of only  $6.0 M_\odot \text{ yr}^{-1}$  is needed to match the observed spectrum. However, the galaxy was modelled as a spherically symmetric system, and the galaxy appears disc-like from the GALFIT analysis in Sec. 3.6. For such a disc-like system, the escape fraction will be significantly lower when observed edge-on, which indeed seems to be the case here.

### 3.8 Star Formation Rate

The F606W flux of the galaxy as measured from the HST data corresponds to a rest frame wavelength of  $1775 \text{ \AA}$  at the redshift of the galaxy. Based on the AB magnitude obtained from our GALFIT analysis (see Table 4) we get a luminosity after correcting for Galactic extinction. We use the emission redshift,  $z_{\text{em}} = 2.3537$ , to compute the luminosity distance. This gives a luminosity of  $L_\nu = F_\nu 4\pi d_L^2 (1+z)^{-1} = 9.63 \times 10^{28} \text{ erg s}^{-1} \text{ Hz}^{-1}$ . We use the extinction correction factor for the F606W band,  $\Delta\text{mag} =$

−0.11 mag, from the NASA/IPAC Extragalactic Database<sup>2</sup> (NED). This luminosity corresponds to a star formation rate of  $\text{SFR}_{\text{UV}} = 13.5 \pm 0.5 M_{\odot} \text{ yr}^{-1}$  using the relation from Kennicutt (1998).

For the  $\text{H}\alpha$  emission line we take the observed line flux (see table 1), which corresponds to a luminosity of  $L_{\text{H}\alpha} = 2.40 \pm 0.10 \times 10^{42} \text{ erg s}^{-1}$ . Converting the luminosity into SFR again using Kennicutt (1998) gives  $\text{SFR}_{\text{H}\alpha} = 18.9 \pm 0.8 M_{\odot} \text{ yr}^{-1}$ .

The discrepancy between the two inferred star formation rates indicates some degree of dust extinction. To quantify the amount of extinction we assume that the two measures should yield the same value, when corrected for dust reddening. The correction factor to the SFR can be expressed as:

$$\text{SFR}_{\text{int}} = \text{SFR}_{\text{obs}} \cdot 10^{0.4 \cdot E(B-V)k(\lambda)}.$$

Requiring that the two SFRs from UV and  $\text{H}\alpha$  be equal we arrive at the following expression:

$$E(B-V) = \frac{2.5}{k(\text{UV}) - k(\text{H}\alpha)} \cdot \log \left( \frac{\text{SFR}_{\text{H}\alpha}}{\text{SFR}_{\text{UV}}} \right),$$

where  $k(\text{UV})$  and  $k(\text{H}\alpha)$  denote the Calzetti et al. (2000) extinction curve evaluated at the UV rest frame wavelength, 1755 Å, and at the rest frame wavelength of  $\text{H}\alpha$ , respectively. From this relation we derive a colour excess of  $E(B-V) = 0.06 \pm 0.01$  consistent with the previously mentioned measure from the Balmer decrement (sect. 3.3). The extinction corrected star formation rate is  $\text{SFR} = 22.8 \pm 1.2 M_{\odot} \text{ yr}^{-1}$  with an assumed Salpeter initial mass function (IMF). If we convert this to the Chabrier IMF we get  $\text{SFR}_{\text{ch}} = 12.7 \pm 0.7 M_{\odot} \text{ yr}^{-1}$ . This measurement agrees very well with the results of Fynbo et al. (2010) and Péroux et al. (2012) who find SFRs of  $\text{SFR} > 10 M_{\odot} \text{ yr}^{-1}$  and  $\text{SFR} = 17.1 \pm 6.0 M_{\odot} \text{ yr}^{-1}$ , respectively.

We note that the two proxies for star formation do not trace star formation on the same physical time-scales, and therefore do not necessarily have to yield the same measured quantity. The  $\text{H}\alpha$ -line primarily traces the ongoing star formation responsible for ionizing the H II-regions, whereas the UV continuum traces previous star formation as well, linked to the O and B stars already in place. However, the young, UV-bright stars may also contribute to photoionization of the gas, and the quantification of the difference depends on assumptions about IMF, star formation history, and the distribution of dust. The detailed, exact modelling of all these factors is beyond the scope of our simple extinction estimate, we have therefore chosen to neglect this effect in the above analysis.

The star formation rate can also be determined directly from the absorption lines associated with the DLA if the  $\text{C II}^*$  absorption line is available (the method is described in Wolfe et al. 2003). Unfortunately the line is blended, so we cannot put any firm constraint on the star formation using this method.

### 3.9 Broad-Band SED Fitting

We fit the three broad-band photometric points from the *HST* imaging mentioned in Sect. 3.6 to obtain estimates of stellar mass, age and star formation rate. But first, we apply a correction for Galactic extinction available from the NED online database<sup>2</sup>. To simplify the fit we subtract the emission-line fluxes from the broad-band fluxes and fit the continuum only, instead of fitting both continuum

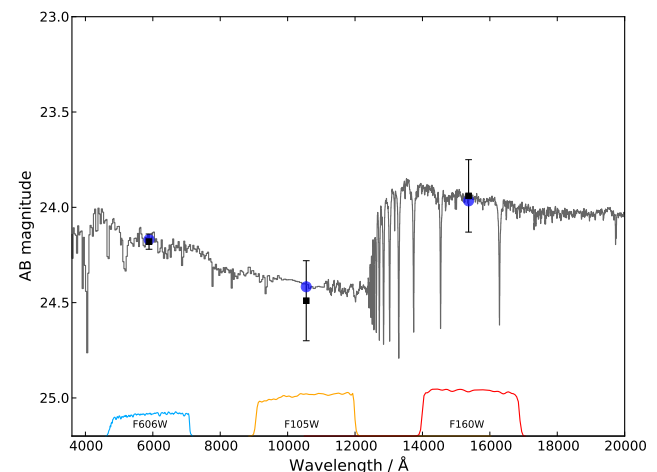


**Figure 7.** Best fitting template (in grey) to our three broad-band photometric points (black, squares). The error-bars in y-direction indicate the  $1\sigma$ -uncertainty on the fluxes. In the bottom of the figure the transmission curves for each filter are shown, and the blue, round points indicate the model magnitudes calculated in each filter passband. The median age and mass of the fit is  $t = 98 \text{ Myr}$  and  $M_{\star} = 2.1 \cdot 10^9 M_{\odot}$ , respectively.

and emission lines simultaneously. The only filter which is influenced by strong emission lines is the F160W band, which contains flux from  $\text{H}\beta$  and the two  $[\text{O III}]$  lines. In order to subtract the emission lines, we assume a flat continuum spectrum, since we only detect the emission lines, and subtract the integrated line fluxes from the total flux in the observed band, weighted by the filter curve. We find that the emission lines contribute 33% of the total flux, and we infer a corrected F160W magnitude of  $m_{160} = 23.94 \pm 0.19$ .

Our fitting code uses the stellar population templates from Bruzual & Charlot (2003) convolved with a large Monte Carlo library of star formation histories (exponential plus random bursts) assuming a Chabrier (2003) IMF. Dust is added following the two-component model of Charlot & Fall (2000), with the parameters being the total optical depth,  $\tau_v$ , and the fraction of dust contributed by the ISM,  $\mu^3$ . We restrict the range of metallicities of the models to be consistent with our measurement from the emission lines  $\log(Z/Z_{\odot}) = -0.3 \pm 0.1$ . We then adopt a Bayesian approach by comparing the observed photometry to the one predicted by all the models in the library, and we construct the probability density functions of stellar mass, mean light-weighted stellar age, and star formation rate. Taking the mean and 16<sup>th</sup> and 84<sup>th</sup> percentiles of the PDF we obtain a stellar mass of  $M_{\star} = 2.1^{+1.4}_{-0.9} \times 10^9 M_{\odot}$ , age of the galaxy of  $t = 98^{+113}_{-48} \text{ Myr}$ , and a star formation rate of  $\text{SFR} = 8.4^{+4.3}_{-1.4} M_{\odot} \text{ yr}^{-1}$ . We also get an estimate of the dust extinction from the fit by comparing the intrinsic template with the best fitting reddened template. From this we infer  $A_V = 0.08^{+0.29}_{-0.07}$ , which corresponds to  $E(B-V) = 0.02^{+0.07}_{-0.02}$ .

The SFR from the SED fit agrees well with the one inferred in Sect. 3.8 within  $1\sigma$ , and also the median value of the dust is consistent with what we find in Sect. 3.3 and 3.8. The photometry and best fitting template are shown in Fig. 7.

<sup>3</sup> For details on the prior distribution of the SFH and dust parameters see Salim et al. (2005)

<sup>2</sup> <http://ned.ipac.caltech.edu/>

## 4 DISCUSSION

### 4.1 Abundances

We have presented a measurement of the gas-phase metallicity in the H II regions of the emission counterpart of the DLA towards the quasar Q 2222–0946. The metallicity we infer using the R<sub>23</sub> and N2 diagnostics expressed in Solar units is [O/H] = −0.30 ± 0.13. From the absorbing gas located 6.3 kpc away, we find a metallicity in the neutral ISM from sulfur of [S/H] = −0.49 ± 0.05, thus slightly lower than the metallicity inferred from the central emitting region. Sulfur is not depleted onto dust, and thereby traces the overall metallicity very well. We find a consistent metallicity from [Si/H] = −0.54 ± 0.05 and [Zn/H] = −0.38 ± 0.05 (note that [Zn/H] is probably overestimated by 0.1 dex). Neither Zn nor Si are significantly depleted onto dust and hence provide a good measurement of the gas-phase metallicity (Meyer & Roth 1990; Pettini et al. 1997). The observed metallicities of DLAs at these redshifts range from [M/H] ≈ −2.5 to [M/H] ≈ −0.2 with an average metallicity weighted by N<sub>H I</sub> of −1.1 ± 0.1 (Rafelski et al. 2012). The DLA in our study is thus amongst the most metal-rich DLAs at this redshift.

From the elements Mn, Fe and Ni we clearly see that dust depletion is in fact at play, the metallicities are [Fe/H] = −1.0, [Ni/H] = −0.9, and [Mn/H] = −1.2, indicating that the refractory elements are, to some degree, removed from the gas-phase, which is to be expected in a high-metallicity system as this particular one (Ledoux et al. 2003). Also, we report a tentative detection of molecular hydrogen, see Sect. 3.5.1.

Bowen et al. (2005) find similar results regarding gas phase metallicities for a low-redshift galaxy, where a quasar intersects the galaxy 3 kpc from a star forming region. The authors find consistent metallicities based on the emission region and the absorbing, neutral gas, respectively. For a compilation of systems with emission and absorption based metallicities, see Péroux et al. (2012).

The presence of highly enriched material 6 kpc above (almost perpendicular to) the galactic plane of this galaxy with nearly the same metallicity as the star forming regions within the galaxy indicates that metal-rich material has been expelled from the galaxy into the halo. We see independent evidence for outflowing gas from the Ly $\alpha$  emission line with a velocity of 160 km s<sup>−1</sup>, see Sect. 3.7 for details. At this velocity we estimate that it would take of the order of 40 Myr for this enriched material to reach a distance of 6.3 kpc from the galaxy plane. Given this relatively short time-scale it seems reasonable that the two metallicities are similar, since no large amount of enrichment has had time to occur after the expulsion of the outflowing gas, which is expected to mix with lower metallicity gas further out, lowering the observed metallicity in the absorbing gas. This scenario can be compared to the wind observed in the nearby galaxy M82, where neutral gas and molecules form a filamentary structure in the outflow extending to great distances from the disc (Veilleux et al. 2009; Melioli et al. 2013).

A recent study by Bregman et al. (2013) shows evidence for a similar scenario, where near-Solar metallicity gas of a nearby, edge-on disc galaxy has been detected 5 kpc above the disc with a neutral hydrogen column density of 1.3 × 10<sup>20</sup> cm<sup>−2</sup>. However, as these authors study a local galaxy a direct comparison to high redshift might not be fully valid.

### 4.2 Dynamical Mass

We can use our information about the size of the galaxy and the kinematics, as probed by the emission lines (see FWHM measures

in Table 1), to get an estimate of the dynamical mass of the system. We follow the method described in Rhoads et al. (2013) to estimate the dynamical mass given the measured size and velocity dispersion:

$$M_{\text{dyn}} \approx \frac{4\sigma^2 a_e}{G \sin^2(i)},$$

where  $i$  denotes the inclination of the system with  $i = 90^\circ$  being edge-on. In order to estimate the velocity dispersion of the system we use the FWHM of the emission lines as a probe of the integrated gas-kinematics of the system. We then take a weighted mean of all the measured line-widths, and correct the FWHM for the instrumental resolution (45 km s<sup>−1</sup>). This gives a measure the velocity dispersion of  $\sigma = 49.1 \pm 7.7$  km s<sup>−1</sup>, and we get the size from the GALFIT analysis in physical units:  $a_e = 1.12 \pm 0.06$  kpc (see Table 4).

From the GALFIT analysis we infer an axis ratio of the galaxy of  $b/a = 0.17$ . The system may be described as reasonably disc-like, given the elongated shape, and the fact that we see a value of Sérsic  $n$  very close to 1. Using the results of Haynes & Giovanelli (1984) that disc galaxies on average have axis ratios around 0.1 – 0.2, we conclude that the galaxy in our study is very close to edge-on, even when assuming the lowest intrinsic value of 0.1. We thus adopt a value of  $i = 90^\circ$  and use the fitted half-light semi-major axis for our estimate of the dynamical mass of the system:  $M_{\text{dyn}} \approx 2.5 \times 10^9 M_\odot$ . This estimate should only be considered a rough approximation (valid within a factor of  $\sim 2$ ) as we have assumed the system to be in virial equilibrium, which it may not be.

### 4.3 Stellar Mass

From our SED fit to the broad-band imaging data, we obtain a stellar mass of  $M_\star = 2.1 \times 10^9 M_\odot$ . We can use this measurement to test the recently proposed evolving mass-metallicity relation for DLA systems (Ledoux et al. 2006, see also Møller et al. (2004, 2013); Neeleman et al. (2013)). Using the relation in Møller et al. (2013), which relates emission metallicity and redshift to stellar mass, with our direct measurement of the emission metallicity, we find a stellar mass of  $M_\star = 6^{+9}_{-4} \times 10^9 M_\odot$ . Though the scatter in their relation is substantial ( $\sim 0.38$  dex), the agreement between the relation and our best fit stellar mass from the SED fit is striking.

Moreover, the mass is in very good agreement with the median stellar mass of Lyman Break Galaxies (LBGs) at redshift  $z = 1 - 3$  (Erb et al. 2006). Hathi et al. (2013) find  $M_{\star, \text{LBG}} = 2 \times 10^9 M_\odot$ , and further characterize the general LBG population in terms of median age ( $\sim 125$  Myr), median SFR ( $\sim 15 M_\odot \text{ yr}^{-1}$ ), and median dust extinction ( $E(B - V) \approx 0.15$ ). All, but the median dust extinction, agree well with our inferred quantities. The dust extinction value is, however, still consistent with our value within the errors (see figure 6 of Hathi et al. 2013). The consistency between the galaxy in our study and the general LBG population shows that there is indeed some overlap between galaxies causing DLAs and star-forming galaxies selected with the Lyman break technique at redshifts  $z = 2 - 3$  (Fynbo et al. 2003; Rauch et al. 2008). Nevertheless, it is important to remember that the DLA in question was specifically chosen to have high metallicity, and is of unusually high metallicity; it is an order of magnitude higher than the median metallicity of DLAs at  $z = 2 - 3$ ,  $[M/H] \simeq -1.5$  or 1/30 of Solar (Noterdaeme et al. 2008; Rafelski et al. 2012). The proposed mass-metallicity relation for DLA galaxies (Ledoux et al. 2006),

then supports the original suggestion by Fynbo, Møller, & Warren (1999) that most DLA galaxy counterparts are too faint to be identified via their stellar or nebular emission.

We are further able to infer the expected metallicity from the stellar mass and SFR using the Fundamental Metallicity Relation from the work of Mannucci et al. (2010). Given the expression from these authors we find an oxygen abundance in the range from  $[O/H] = -0.3$  to  $[O/H] = -0.5$ , depending on the fitting function assumed. Since the SFR of our target is slightly outside the range over which the relation is derived there will be uncertainty related to the extrapolation. The metallicity is, however, still in perfect agreement with our measurements. This indicates that the DLA in our study follows the same relation as other galaxies studied at both lower and higher redshifts, strengthening the link between this DLA galaxy and the general population of star-forming galaxies.

### The Tully-Fisher Relation

We now turn to look at how this galaxy is located on the stellar-mass Tully-Fisher relation ( $M_*$ -TFR) to test our assumption that the system is disc-like and relaxed. The Tully-Fisher relation, originally stated in terms of luminosity and velocity (Tully & Fisher 1977), can also be presented in terms of stellar mass (which correlates with luminosity) and velocity. The  $M_*$ -TFR was studied in detail by Kassin et al. (2007) who gave their best fit to the data as:

$$\log(S_{0.5}) = 1.89 \pm 0.03 + 0.34 \pm 0.05 \cdot \log\left(\frac{M_*}{10^{10} M_\odot}\right),$$

where  $S_{0.5}$  is defined by the authors as  $S_K^2 \equiv K V_{\text{rot}}^2 + \sigma_g^2$ , with  $K = 0.5$ . Using the measured velocity dispersion as a proxy for  $S_{0.5}$  (see a discussion of this in Rhoads et al. 2013) we find that the inferred stellar mass is  $M_* = 2.6_{-1.2}^{+1.9} \times 10^9 M_\odot$ . This is in very good agreement with our previously mentioned mass estimates, including our rough estimate of the dynamical mass.

The stellar (and dynamical) mass inferred from the emission line widths is subject to uncertainties caused by the fact that we do not know the detailed structure of the velocity field. The emission lines are most certainly influenced by turbulence in the gas, which we cannot quantify. This would overestimate our line-widths and thereby our TF-based stellar mass and dynamical mass estimates. Also, we required that the system be in virial equilibrium; however, we observe gas at large galactocentric radii, almost perpendicular to the disc, with similar metallicity as the line emitting region, indicating outflowing gas from the central parts. This has an impact on our calculation of the dynamical mass, and our ability to use the line-widths as a tracer of the ordered rotation of the system. Moreover, a non-negligible gas mass is expected in a young ( $\sim 100$  Myr), star-forming galaxy. This mass would not be accounted for in the stellar mass estimate from the SED fit, but would contribute to the dynamical mass, thus increasing the observed velocity dispersion. We estimate the gas mass from the star formation density (see Kennicutt 1998) using the half-light radius and the axis-ratio of the galaxy. We infer a gas mass of  $M_{\text{gas}} = 1_{-0.5}^{+3} \times 10^9 M_\odot$ . This estimate is a very rough approximation given the large scatter ( $\sim 0.3$  dex) in the relation, and is therefore not to be trusted as a true value of the amount of gas. It does, however, indicate that a gas mass of roughly half the stellar mass is present. We note that the inferred dynamical mass is consistent with our best-fit stellar mass within  $1\sigma$ , and a significant gas mass is therefore not required in order to reconcile the two mass estimates, and within the (large) uncertainties, all

three mass estimates agree well. The compact nature of the galaxy also means that the kinematics of the emission lines only probe the innermost region, and are therefore mostly sensitive to the stellar mass concentrated in the central region, and not the gas in the outer parts.

Studies of the TFR at higher redshifts find that the relation is offset to lower stellar masses for a given velocity. We see a similar though not statistically significant trend in our data. Cresci et al. (2009) find that LBGs at  $z \approx 2$  are offset by 0.4 dex compared to the local TFR, and they find that the relation has *low* scatter. Gnerucci et al. (2011) find similar results in their sample of  $z \approx 3$  galaxies with an offset up to 1 dex, however, the scatter in their data is very large. This may indicate that the TFR has not yet been established at these redshifts, and that the galaxies are influenced heavily by random motions.

## 5 SUMMARY AND CONCLUSION

We have presented our analysis of a high-redshift galaxy selected from its neutral hydrogen absorption seen in the spectrum of a background quasar. We have presented the extracted emission lines from the galaxy counterpart of the absorption, and combined these with our detailed absorption-line study to probe the metallicities seen in the two phases. We find that the two metallicities are similar, but the absorbing gas has a slightly lower metallicity than the emitting gas. We use *HST* imaging to constrain the stellar population; our data are consistent with the picture in which the galaxy causing the Ly $\alpha$  absorption is a young, small ( $\sim 1$  kpc), disc-like system, with a not fully ordered (proto-) disc structure. Moreover, we see evidence for a so-called *galactic fountain*, where enriched gas gets blown out from the star-forming regions, forms the neutral hydrogen absorption that we see  $\sim 6$  kpc above the galactic plane, and in the end may settle back onto the disc.

This galaxy demonstrates exactly how star-forming galaxies at high redshift may overlap with the population of the most metal-rich DLAs. However, the very faint nature of damped Lyman- $\alpha$  absorbing galaxies renders the majority of these almost impossible to detect. The few exceptions, such as the case reported here, thus offer a rare glimpse into this elusive galaxy population.

## ACKNOWLEDGEMENTS

We thank the anonymous referee for the a nice and constructive report. The Dark Cosmology Centre is funded by the DNRF. JPUF and PL acknowledge support from the ERC-StG grant EGG-278202. JK acknowledges support from an ESO Studentship. CP has benefited from support of the Agence Nationale de la Recherche with reference ANR-08-BLAN-0316-01. This research has made use of the NASA/IPAC Extragalactic Database (NED) which is operated by the Jet Propulsion Laboratory, California Institute of Technology, under contract with the National Aeronautics and Space Administration. The RT simulations were conducted on the facilities provided by the Danish Center for Scientific Computing. A.G. acknowledges support from the EU FP7/2007-2013 under grant agreement n. 267251 AstroFit.

## REFERENCES

- Asplund, M., Grevesse, N., Sauval, A. J., & Scott, P., 2009, *ARA&A*, 47, 481

- Bowen, D. V., Jenkins, E. B., Pettini, M., & Tripp, T. M., 2005, *ApJ*, 635, 880
- Bregman, J. N., Miller, E. D., Seitzer, P., Cowley, C. R., & Miller, M. J., 2013, *ApJ*, 766, 57
- Bruzual, G. & Charlot, S., 2003, *MNRAS*, 344, 1000
- Caffau, E., Bonifacio, P., François, P., et al., 2011, *A&A*, 534, A4
- Calzetti, D., Armus, L., Bohlin, R. C., Kinney, A. L., Koorneef, J., & Storchi-Bergmann, T., 2000, *ApJ*, 533, 682
- Chabrier, G., 2003, *Publications of the Astronomical Society of the Pacific*, 115, 763
- Charlot, S. & Fall, S. M., 2000, *ApJ*, 539, 718
- Cresci, G., Hicks, E. K. S., Genzel, R., et al., 2009, *ApJ*, 697, 115
- Erb, D. K., Shapley, A. E., Pettini, M., Steidel, C. C., Reddy, N. A., & Adelberger, K. L., 2006, *ApJ*, 644, 813
- Fontana, A. & Ballester, P., 1995, *The Messenger*, 80, 37
- Frebel, A., Johnson, J. L., & Bromm, V., 2007, *MNRAS*, 380, L40
- Frebel, A., Simon, J. D., Geha, M., & Willman, B., 2010, *ApJ*, 708, 560
- Fynbo, J. P. U., Laursen, P., Ledoux, C., et al., 2010, *MNRAS*, 408, 2128
- Fynbo, J. P. U., Ledoux, C., Møller, P., Thomsen, B., & Burud, I., 2003, *A&A*, 407, 147
- Fynbo, J. P. U., Ledoux, C., Noterdaeme, P., et al., 2011, *MNRAS*, 413, 2481
- Fynbo, J. P. U., Starling, R. L. C., Ledoux, C., et al., 2006, *A&A*, 451, L47
- Fynbo, J. U., Møller, P., & Warren, S. J., 1999, *MNRAS*, 305, 849
- Gnerucci, A., Marconi, A., Cresci, G., et al., 2011, *A&A*, 528, A88
- Hathi, N. P., Cohen, S. H., Ryan, Jr., R. E., et al., 2013, *ApJ*, 765, 88
- Haynes, M. P. & Giovanelli, R., 1984, *AJ*, 89, 758
- Holmberg, J., Nordström, B., & Andersen, J., 2007, *A&A*, 475, 519
- Horne, K., 1986, *PASP*, 98, 609
- Kassin, S. A., Weiner, B. J., Faber, S. M., et al., 2007, *ApJ*, 660, L35
- Kelvin, L. S., Driver, S. P., Robotham, A. S. G., et al., 2012, *MNRAS*, 421, 1007
- Kennicutt, Jr., R. C., 1998, *ARA&A*, 36, 189
- Kewley, L. J. & Ellison, S. L., 2008, *ApJ*, 681, 1183
- Kobulnicky, H. A. & Kewley, L. J., 2004, *ApJ*, 617, 240
- Krogager, J.-K., Fynbo, J. P. U., Møller, P., Ledoux, C., Noterdaeme, P., Christensen, L., Milvang-Jensen, B., & Sparre, M., 2012, *MNRAS*, 424, L1
- Kudritzki, R.-P., Urbaneja, M. A., Gazak, Z., Bresolin, F., Przybilla, N., Gieren, W., & Pietrzyński, G., 2012, *ApJ*, 747, 15
- Laursen, P., Duval, F., & Östlin, G., 2013, *ApJ*, 766, 124
- Laursen, P., Razoumov, A. O., & Sommer-Larsen, J., 2009a, *ApJ*, 696, 853
- Laursen, P., Sommer-Larsen, J., & Andersen, A. C., 2009b, *ApJ*, 704, 1640
- Ledoux, C., Petitjean, P., Fynbo, J. P. U., Møller, P., & Srianand, R., 2006, *A&A*, 457, 71
- Ledoux, C., Petitjean, P., & Srianand, R., 2003, *MNRAS*, 346, 209
- Mannucci, F., Cresci, G., Maiolino, R., Marconi, A., & Gnerucci, A., 2010, *MNRAS*, 408, 2115
- Melioli, C., de Gouveia Dal Pino, E. M., & Geraissate, F. G., 2013, *MNRAS*, 430, 3235
- Meyer, D. M. & Roth, K. C., 1990, *ApJ*, 363, 57
- Modigliani, A., Goldoni, P., Royer, F., et al., 2010, in *Society of Photo-Optical Instrumentation Engineers (SPIE) Conference Series*, Vol. 7737, Society of Photo-Optical Instrumentation Engineers (SPIE) Conference Series
- Møller, P., Fynbo, J. P. U., & Fall, S. M., 2004, *A&A*, 422, L33
- Møller, P., Fynbo, J. P. U., Ledoux, C., & Nilsson, K. K., 2013, *MNRAS*, 430, 2680
- Neeleman, M., Wolfe, A. M., Prochaska, J. X., & Rafelski, M., 2013, *ApJ*, 769, 54
- Noterdaeme, P., Laursen, P., Petitjean, P., et al., 2012, *A&A*, 540, A63
- Noterdaeme, P., Ledoux, C., Petitjean, P., & Srianand, R., 2008, *A&A*, 481, 327
- O'Rourke, D. J. P., Shabala, S. S., & Alexander, P., 2011, *MNRAS*, 418, 2145
- Pagel, B. E. J., Edmunds, M. G., Blackwell, D. E., Chun, M. S., & Smith, G., 1979, *MNRAS*, 189, 95
- Peng, C. Y., Ho, L. C., Impey, C. D., & Rix, H.-W., 2002, *AJ*, 124, 266
- Péroux, C., Bouché, N., Kulkarni, V. P., York, D. G., & Vladilo, G., 2012, *MNRAS*, 419, 3060
- Pettini, M., 2006, in *The Fabulous Destiny of Galaxies: Bridging Past and Present*, Le Brun, V., Mazure, A., Arnouts, S., & Burgarella, D., eds., p. 319
- Pettini, M., King, D. L., Smith, L. J., & Hunstead, R. W., 1997, *ApJ*, 478, 536
- Pettini, M. & Pagel, B. E. J., 2004, *MNRAS*, 348, L59
- Prochaska, J. X., Chen, H.-W., Dessauges-Zavadsky, M., & Bloom, J. S., 2007, *ApJ*, 666, 267
- Rafelski, M., Wolfe, A. M., Prochaska, J. X., Neeleman, M., & Mendez, A. J., 2012, *ApJ*, 755, 89
- Rauch, M., Haehnelt, M., Bunker, A., et al., 2008, *ApJ*, 681, 856
- Rhoads, J. E., Malhotra, S., Finkelstein, S. L., Fynbo, J. P. U., McLinden, E. M., Richardson, M. L. A., & Tilvi, V. S., 2013, *ArXiv e-prints*, 1301.3140
- Salim, S., Charlot, S., Rich, R. M., et al., 2005, *ApJ*, 619, L39
- Savaglio, S., 2006, *New Journal of Physics*, 8, 195
- Shapley, A. E., 2011, *ARA&A*, 49, 525
- Tully, R. B. & Fisher, J. R., 1977, *A&A*, 54, 661
- Veilleux, S., Rupke, D. S. N., & Swaters, R., 2009, *ApJ*, 700, L149
- Vernet, J., Dekker, H., D'Odorico, S., et al., 2011, *A&A*, 536, A105
- Wolfe, A. M., Gawiser, E., & Prochaska, J. X., 2005, *ARA&A*, 43, 861
- Wolfe, A. M., Prochaska, J. X., & Gawiser, E., 2003, *ApJ*, 593, 215
- Zafar, T. & Watson, D., 2013, *arXiv:1303.1141*